# Exploring the Symmetries of Pantropical Connections between the Tropical Atlantic and Pacific Basins

RAJASHREE NAHA,[a,b] SHAYNE MCGREGOR,[a,b] AND MARTIN SINGH[a,b]

[a] *School of Earth Atmosphere and Environment, Monash University, Melbourne, Victoria, Australia*
[b] *Australian Research Council Centre of Excellence for Climate Extremes, Monash University, Melbourne, Victoria, Australia*

(Manuscript received 14 May 2022, in final form 7 April 2023, accepted 12 April 2023)

ABSTRACT: Recent analysis of pantropical interactions suggests that after 1980 the tropical Atlantic Ocean's (TAO) influence on the tropical Pacific Ocean (TPO) appears to have become much more pronounced while the tropical Indian Ocean's (TIO) influence appears to have weakened. This study explores whether and how decadal changes in TAO and TPO SSTs modulate these pantropical connections in an attempt to explain the recent dominance of the TAO. To this end, we carry out a series of idealized atmosphere-only experiments using the ACCESS atmospheric general circulation model where the magnitude and sign of the decadal TAO SST signal are varied, presenting various warm and cool Atlantic scenarios. To understand further if these pantropical connections are influenced by changes in TPO SST, we carry out the above TAO experiments with both warm and cool phases of Pacific decadal variability (PDV). We find that an imposed TAO warming leads to increases in TPO atmospheric temperature and stability, which lead to a decrease in average TPO precipitation, with the most prominent changes occurring in June–August. These changes in TPO precipitation induced by TAO warming are largely mirrored when TAO cooling is added, whereas the TPO rainfall response to TAO anomalies remains relatively unchanged for the different phases of PDV. In contrast to the precipitation response, the wind response did display some asymmetries between different phases of TAO SST variability. Specifically, surface winds in the western half of the Niño-4 region exhibited a significantly different response to positive versus negative Atlantic multidecadal variability (AMV), whereas the surface winds in the western equatorial Pacific were significantly stronger (roughly 40% larger) in the positive phase of PDV than in the negative phase. These results suggest that the phases of PDV and AMV may modulate pantropical interactions through their effect on zonal wind stress.

KEYWORDS: Atlantic Ocean; Teleconnections; ENSO; Climate models; Climate variability; Tropical variability

## 1. Introduction

The tropical Pacific Ocean (TPO) is home to the globe's most dominant mode of interannual climate variability, El Niño–Southern Oscillation (ENSO). ENSO is a coupled ocean–atmosphere phenomenon that results from positive feedback between anomalous western Pacific (WP) zonal winds and eastern equatorial Pacific sea surface temperature (SST), that is, the Bjerknes feedback (Bjerknes 1969). ENSO oscillates between two phases roughly every 3–7 yr: El Niño phase, in which above-average SSTs are observed across the central-eastern equatorial Pacific, and La Niña phase, in which below-average SSTs are observed in that region. A shift in the phase of ENSO is associated with a large-scale reorganization of tropical precipitation, and it is accompanied by global impacts on society and the economy (McPhaden et al. 2006).

The magnitude, frequency, and characteristics of ENSO variability itself vary on multidecadal time scales, with a number of large-magnitude ENSO events occurring in the 1980s and 1990s (Trenberth and Hoar 1997; Timmermann et al. 1999, 2018) and lower-amplitude, but more frequent, events being observed in the recent period (Maher et al. 2014, 2018; Wang et al. 2019). Decadal and longer time-scale changes in the background-state SSTs of the Pacific Ocean [herein, Pacific decadal variability (PDV)] have been shown to be important for understanding changes in ENSO and its behavior (Cai et al. 2001; McPhaden et al. 2020; Karamperidou et al. 2020), although the exact drivers of these background-state changes and their relationship to ENSO remain unresolved (e.g., Power et al. 2021). Furthermore, these background-state changes in the Pacific play an important role in modulating the magnitude of global warming. For instance, it is reported that the recent acceleration of the trade winds was associated with cooling in the central and eastern Pacific (EP), contributing to the recent "hiatus" of global warming (Kosaka and Xie 2013; England et al. 2014).

Recent research indicates that there is a two-way interaction between tropical Pacific variability and that in other basins. That is, the tropical Atlantic Ocean (TAO; 75°W–30°E, 20°N–20°S) and the tropical Indian Ocean (TIO; 30°–130°E, 20°N–20°S) both feed back onto the TPO (130°E–75°W, 20°N–20°S) remotely, just like the Pacific forces the tropical climate variability in them (Kug and Kang 2006; Ham et al. 2013; Li et al. 2016; Wang et al. 2017). These pantropical interactions are increasingly considered to be integral to understanding background-state changes in the tropical Pacific and predicting the El Niño properties (Ohba and Ueda 2007; Luo et al. 2012; Ham et al. 2013; Dommenget and Yu 2017; Chikamoto et al. 2016; Li et al. 2021).

Our focus here is on the tropical Atlantic–Pacific connections, with a general focus on the North Atlantic due to the prominent multidecadal SST changes recently observed here [herein, Atlantic multidecadal variability (AMV)]. Previous

*Corresponding author*: Rajashree Naha, rajashree.naha@monash.edu

DOI: 10.1175/JCLI-D-22-0355.1

studies have suggested a number of pathways by which AMV affects the Pacific. For instance, a positive phase of AMV, or a warm North Atlantic, has been associated with an increased prevalence of biennial central Pacific ENSO events (Wang et al. 2017; Ding et al. 2023). Further, the warming of the Atlantic since the early 1990s has been reported to play a crucial role in background-state changes in the Pacific, with a corresponding acceleration of the Pacific trade winds and cooling in the central and eastern Pacific, consistent with the negative phase of PDV (McGregor et al. 2014; Ruprich-Robert et al. 2017). This Pacific decadal response to Atlantic warming is consistent with expectations from a Matsuno–Gill-type response (Gill 1980), which directly connects the Atlantic SSTs with the Pacific Walker circulation (Li et al. 2016).

The interannual and decadal pantropical interactions between the tropical Atlantic and Pacific appear to have grown stronger since the late 1990s with the warming of the North Atlantic (Cai et al. 2019), which is at least partly linked to AMV (Choi et al. 2019). Indices of pantropical interactions that quantify the relationships between decadal SST changes between different basins (Cai et al. 2019) show that, before 1980, both the TIO and TAO appeared to influence the Pacific to a similar degree, with both the TAO–TPO and TIO–TPO SST difference trends being well correlated with western tropical Pacific zonal wind stress trends. Since 1980, however, indices of western tropical Pacific zonal wind stresses are more strongly correlated with the TAO–TPO SST difference than with the TIO–TPO SST difference, suggesting that either internal climate system noise may influence these correlations (Yun and Timmermann 2018) or the strength of the influence of different basins on the TPO may have changed with time (Cai et al. 2019). Simulations with partially coupled models have confirmed some aspects of the latter, but the mechanisms responsible for the dominance of different basins at different times are still not fully understood (Meehl et al. 2021).

The easiest explanation for the changing strength of pantropical connections is that the TAO–TPO SST differences experienced in the recent period are larger than those of the past. However, observed time series of this index during the historical period reveal that TAO–TPO SST differences of similar magnitude have been experienced in the past (McGregor et al. 2014; Fig. 3), making this explanation unlikely. Thus, this study utilizes a series of forced atmospheric general circulation model (AGCM) simulations to explore solutions to the following research questions:

1) Does the TPO response to TAO SST changes vary with the seasons or the sign and magnitude of the TAO SST changes?
2) What are the dynamics underlying these connections, and does the TAO–TPO connection vary with the phase of PDV?

Specifically, we use an AGCM to examine the impact of recent Atlantic Ocean SST changes and their inverse while leaving the TPO SSTs unchanged. To this end, we simulate the influence of positive and negative AMV phases of different magnitudes on the Pacific basin atmospheric response, also experimenting with both positive and negative phases of PDV. This experimental design allows us to understand the pantropical response without having to consider the TPO changes that would invariably come about in the coupled setting.

This paper is organized as follows: section 2 details the model and experimental design, section 3 describes the tropical Pacific basinwide rainfall response and reports on the dynamics of rainfall changes, section 4 illustrates the regional response of precipitation, section 5 describes the regional wind response and its relationship to TPO precipitation changes, and section 6 presents the study's conclusions.

## 2. Model and experiment design

To determine the effects of TAO SST anomalies (SSTAs) on the Pacific basin atmospheric circulation, including whether the Pacific response varies with the season or the sign and magnitude of the TAO SST changes, we carry out a series of Atmospheric Model Intercomparison Project (AMIP)–style (prescribed SSTs) experiments with the Australian Community Climate and Earth-System Simulator (ACCESS), version 1.3b, AGCM (atmosphere and land surface only). A more detailed description of the ACCESS model is given in Bi et al. (2013). The model is run on a 1.25° × 1.875° horizontal grid with 38 levels in the vertical. Each of our simulations covers the period between 1978 and 2001 based on the AMIP-II method of updating SSTs (Taylor et al. 2000) and includes 10 ensemble members. In all simulations, external forcings (aerosols, greenhouse gases, etc.) are temporally evolving, and daily and monthly average outputs are saved.

We initially carry out five sets of experiments that seek to understand the extent to which SST anomalies in the TAO are able to modulate the Pacific atmospheric background state. Each of these five experiments has the same SST forcing in the Pacific and Indian Ocean but has a different temporally fixed pattern of SSTAs (Figs. 1a,b) added to the climatology in the Atlantic region. The SST pattern that is applied to the TAO is concentrated only within the tropics (30°S–30°N) and tapers out linearly over 31°–34° north and south as we move poleward, while climatological SSTs have been imposed outside the tropics. In the TPO, the imposed SSTs are temporally evolving and taken from the AMIP-simulated SST (Taylor et al. 2000) for the period 1978–2001. In the IO, the SSTs do not evolve with time and are given by the climatology calculated over the 1978–2001 period. Note that the IO region is separated from the PO region via the Asian (north), Maritime (center), and Australian (south) continents, so the influence of the induced SST gradients between the two ocean basins should be minimal. The fixed pattern of TAO SSTAs is calculated as the difference between the 1982–98 and 1999–2014 mean SSTs (Figs. 1a,b). This pattern is consistent with those that have previously been proposed as key modulators of the background state of the Pacific basin (McGregor et al. 2014, 2018; Li et al. 2016; Ruprich-Robert et al. 2017). This fixed TAO SSTA pattern is then multiplied by a constant, $\alpha$ ($\alpha = -1$, $-1/2$, 0, $1/2$, and 1), and added to the climatological TAO SST forcing (1978–2001), rendering our five experiments. The $\alpha = 0$ case is our "PDV+ control" experiment, where PDV+ refers

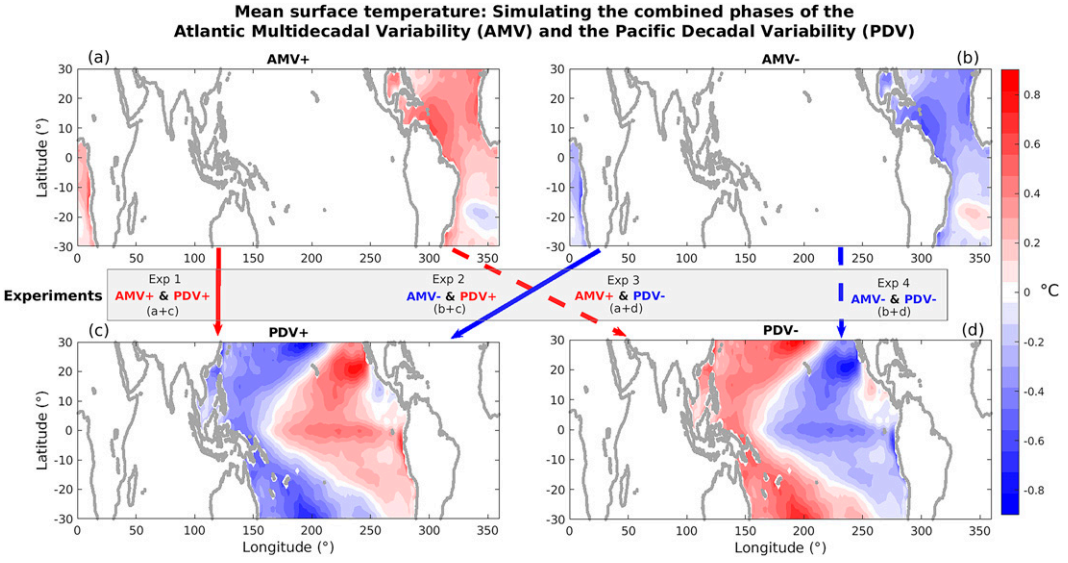


FIG. 1. Mean SSTA (°C) for the JJA season in (a) AMV+ minus control and (b) AMV− minus control. Also shown are the two phases of PDV: (c) PDV+ and (d) PDV−. Different colored arrows represent the combination of AMV and PDV phases utilized in our experiments, where the color (red or blue) refers to the AMV phase (positive or negative, respectively), solid lines refer to the PDV+ phase, and dashed lines refer to the PDV− phase.

to the fact that the majority of the 1978–2001 period occurs in the PDV-positive phase (Mantua and Hare 2002; Newman et al. 2016). Of the four remaining experiments, the two negative AMV cases ($\alpha = -1$ and $-0.5$) correspond to Atlantic cooling (PDV+ AMV− and PDV+ 0.5AMV−, respectively), whereas the two positive AMV cases ($\alpha = +1$ and $+0.5$) correspond to Atlantic warming (PDV+ AMV+ and PDV+ 0.5AMV+, respectively), as illustrated in Fig. 1. Our experiments are designed in such a way that any induced SST gradient within the TIO or TPO would also appear in the control and thus would be removed when calculating anomalies (experiment minus control).

To understand if the tropical Atlantic–Pacific connection is influenced by the PDV phase, we carry out an additional set of five experiments similar to those described above. However, here we change the phase of PDV during this period by adding SSTAs from the negative PDV phase on the TPO, where the SSTA pattern is calculated as the SST difference between 1998–2014 and 1982–98 (Fig. 1d). This decadal difference also marks the difference between two phases of the Pacific interdecadal oscillation. As above, each of these five experiments has the same SSTA forcing in the TPO and TIO, while the fixed SSTA (Figs. 1a,b) applied to the Atlantic region is multiplied by a constant, $\alpha$ ($\alpha = -1$, $-1/2$, 0, $1/2$, and 1), and then added to the climatological TAO SST forcing (1978–2001). The $\alpha = 0$ case is our "PDV− control" experiment. As above, the two negative cases ($\alpha = -1$ and $-0.5$) correspond to Atlantic cooling (PDV− AMV− and PDV− 0.5AMV−, respectively), whereas the two positive cases ($\alpha = +1$ and $+0.5$) correspond to Atlantic warming (PDV− AMV+ and PDV− 0.5AMV+, respectively), as illustrated in Fig. 1.

Combined, these 10 AMIP-style experiments allow us to examine the impact of TAO SSTAs on the TPO and whether these impacts are modulated by the PDV phase.

## 3. The basinwide rainfall response

### a. *Rainfall changes*

We first consider the TAO response of rainfall in the AMV experiments. We plot the long-term average seasonal cycle of TAO mean precipitation differences between the Atlantic experiments (i.e., AMV+ and AMV−) and the respective control simulations. This reveals that the AMV+ experiments enhance Atlantic rainfall, while the AMV− experiments suppress Atlantic rainfall (Figs. 2a–c). These rainfall differences are found to be largest in the May–November months.

Of particular interest to understanding how pantropical connections have varied in time is the extent to which the response of the atmosphere to TAO variability is asymmetric between different phases of AMV or different depending on the phase of PDV, for example, whether the AMV+ experiment produces a rainfall response that differs in magnitude to the AMV− experiment. We assess asymmetry in the AMV phase here and elsewhere in this paper by determining if the response in the AMV+ experiment is significantly different to the response in the AMV− experiment with its sign flipped. Here, significance is taken at the 95th percentile confidence using a Student's $t$ test. Similarly, we assess differences between PDV phases by determining whether there is a statistically significant difference in the response to AMV anomalies when under the PDV+ phase versus under the PDV− phase. We note here that the basinwide average AMV and

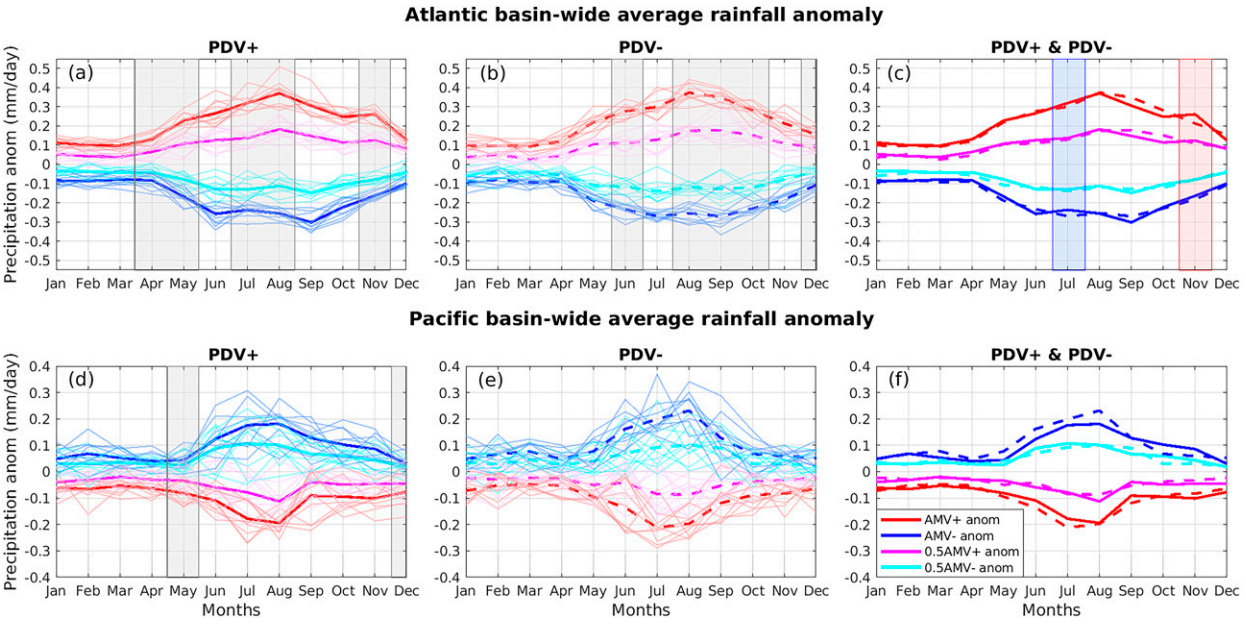


FIG. 2. Seasonal cycle of the mean precipitation anomalies (1978–2001) over the (a)–(c) tropical Atlantic basin (75°–15°W, 20°N–20°S) – and (d)–(f) tropical Pacific basin (130°E–75°W, 20°N–20°S)–. Anomalies from each AMV experiment (with respect to the relevant PDV phase control simulation) are marked by different colors (see the legend); thin lines represent individual ensemble members, and thick lines represent the ensemble means. (left) Output from the PDV+ phase, (center) the PDV− output, and (right) the ensemble means of all experiments. The gray shadings in the left and center columns indicate the statistically significant months at 95% confidence interval for the AMV phase asymmetries (i.e., AMV+ vs AMV−), and the colored shadings in the right-hand column indicate the statistically significant months at 95% confidence interval for the PDV phase asymmetries (red shading indicates the difference in the AMV+ experiments between the two PDV phases, and blue shading represents the difference in AMV− experiments between the two PDV phases).

PDV phase asymmetries identified in this section are relatively small.

Using the above test, we find significant AMV phase asymmetries (marked as gray shadings) in the months of April and May, July and August, and November in the PDV+ phase (Fig. 2a) and in the months of June, August–October, and December in the PDV− phase (Fig. 2b). During these months displaying significant AMV phase differences, the AMV+ experiments have a larger-magnitude rainfall response than the AMV− experiments. We also find that the AMV-induced rainfall differences between the PDV phases (Fig. 2c) show significant differences during July and November. In these months, the response to AMV is different in different PDV phases. However, we note that the PDV phase asymmetries are small, suggesting they stem from random chance, or they may also be forced by changes in TPO precipitation.

Next, we consider the remote response of TAO SST anomalies on rainfall over the TPO. We examine the effect of a warm or cool Atlantic (AMV+ or AMV−) on basin-averaged rainfall in the TPO (Figs. 2d–f). On average, the warm TAO experiments (AMV+ and 0.5AMV+ experiments) have lower precipitation over the TPO through all seasons than the control simulations. The AMV− and 0.5AMV− experiment results virtually mirror those of the AMV+ and 0.5AMV+ experiments, with higher precipitation than the control simulations over the TPO. Thus, we see a reduced precipitation response over the TPO for a warmer Atlantic (AMV+ or 0.5AMV+) and an increased precipitation response for a cooler Atlantic (AMV− or 0.5AMV−). The anomalies in the TPO are largest during June–August (JJA) (Figs. 2d–f), despite the rainfall signal being large in the TAO from May to November (Figs. 2a–c). The TPO basinwide rainfall changes are largely linear with respect to AMV and PDV phase and magnitude (Figs. 2d–f). However, there are significant AMV phase differences in the months of May and December in the PDV+ phase (Fig. 2d), where the AMV− experiment has a larger-magnitude precipitation response that the AMV+ experiment. On the other hand, the effect of the imposed TAO SST anomalies on basinwide TPO precipitation is statistically indistinguishable between the PDV+ and PDV− cases (Fig. 2f).

### b. *Dynamics of rainfall changes*

The above Pacific basin rainfall changes may be qualitatively understood by considering a simple linear model of the equatorial response to diabatic heating anomalies (Gill 1980). The Atlantic Ocean warming enhances convection locally, thereby producing a positive diabatic heating anomaly in the troposphere. This heat source results in the production of atmospheric Kelvin and Rossby waves propagating to the east and west of the heat source, respectively (Gill 1980). These waves alter the temperature structure of the entire tropical belt, thereby altering the stability in regions remote from the SST anomalies. This tropicswide tropospheric warming associated

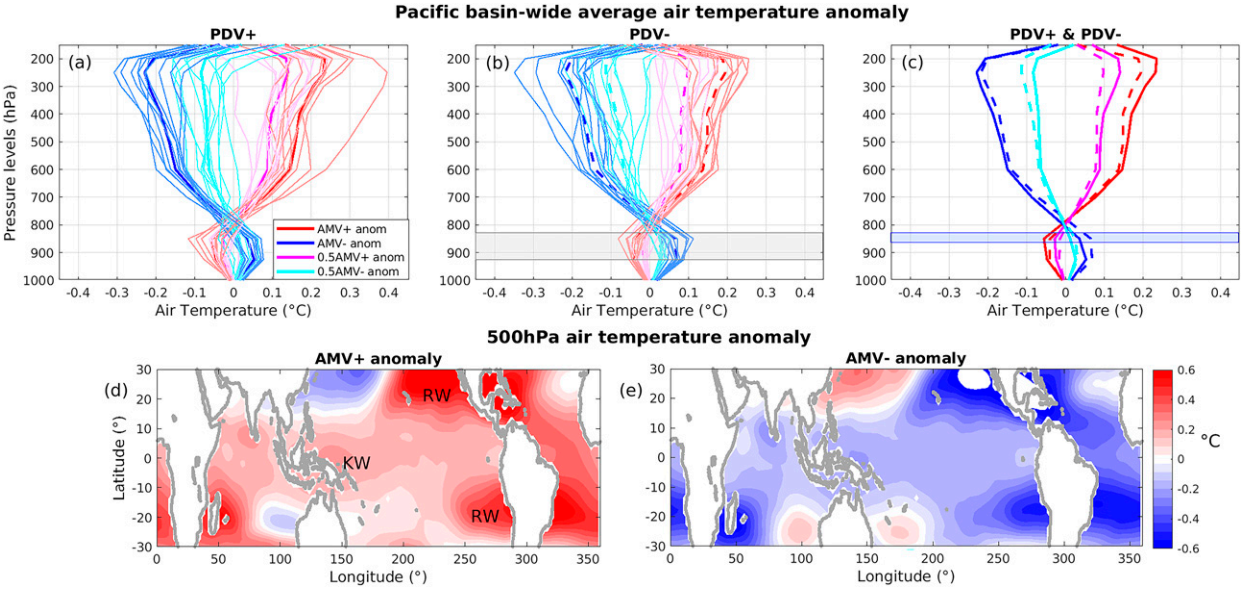


FIG. 3. Atmospheric temperature (°C) anomalies (AMV experiments minus control) vs pressure (hPa) over the TPO for the JJA season in (a) PDV+ and (b) PDV−; (c) PDV+ and PDV− phases plotted together. Also shown are midtropospheric (500 hPa) air temperature anomalies (°C) over the tropical oceans in the JJA season for (d) AMV+ minus control and (e) AMV− minus control. These anomalies are with respect to the relevant PDV phase control simulation. Gray shading indicates statistically significant levels at 95% confidence interval for the AMV phase asymmetries, and colored shading indicates statistically significant levels at 95% confidence interval for the PDV phases asymmetries (red shading indicates that the difference in the AMV+ experiments between the two PDV phases is statistically significant, and blue shading indicates that the difference in AMV− experiments between the two PDV phases is statistically significant).

with Atlantic SST anomalies is consistent with the weak temperature gradient (WTG) approximation (Sobel et al. 2001; Bretherton and Sobel 2003), and the WTG framework provides an alternative conceptual model through which to interpret the pantropical interactions in our simulations. As precipitation is strongly sensitive to atmospheric stability, the resultant changes in atmospheric stability provide a mechanism for the remote response of precipitation in different tropical ocean basins.

To confirm the role of the above mechanism, we examine the changes in the Pacific basin average tropospheric temperature in the different AMV experiments in both PDV phases (Fig. 3). Here, we focus on the June–August period, as this is the period with the most prominent TPO precipitation changes (Figs. 2d–f), but we note that similar results are found for other seasons (not shown). For both the AMV+ and AMV− experiments, the temperature anomalies are small near the surface, which is consistent with each of the experiments having the same imposed TPO SST as the control. However, at levels above 800 hPa, air temperature anomalies for AMV+ (or 0.5AMV+) increase with altitude, thereby creating a more stable atmosphere over the Pacific, leading to decreases in rainfall. For AMV− (or 0.5AMV−), the air temperature above 800 hPa decreases with altitude, causing instability and making conditions favorable for precipitation to occur over the TPO. These atmospheric temperature changes are consistent with the TPO rainfall changes (Fig. 2) and the mechanisms described above. Significant AMV phase asymmetries are apparent, but only at the 925- and 850-hPa model levels in the PDV− phase (Figs. 3a,b). The temperature anomalies induced over the Pacific basin as a result of the imposed TAO SSTs are statistically indistinguishable between the positive and negative PDV phases, except at the 850-hPa level (Fig. 3c).

Figures 3d and 3e show the spatial structure of the temperature anomalies in °C (PDV+ AMV experiments minus the PDV+ control) at 500 hPa over the tropical oceans during JJA. We note here that these spatial structures are largely similar between the PDV phases (not shown), with spatial correlations of 0.93 and 0.95 between the 500-hPa air temperature anomalies of both PDV phases in the AMV+ and AMV− experiments, respectively. These 500-hPa temperature anomalies appear to show signatures of off-equatorial Rossby waves propagating westward of the heat source and equatorial Kelvin waves propagating eastward of the heat source, consistent with a Matsuno–Gill-type response to the Atlantic temperature changes. This is consistent with our previous results (Figs. 2 and 3a–c), suggesting that the local diabatic heating/cooling triggered by the imposed TAO SSTA generates large-scale waves that radiate away from the source throughout the tropics. These waves impact the atmospheric temperature stratification over the TPO, ultimately impacting the region's rainfall. In summary, the troposphere over the TPO is more stable in the AMV+ case, with a resultant reduction in TPO rainfall, and it is less stable in the AMV− case, with a resultant increase in TPO rainfall.

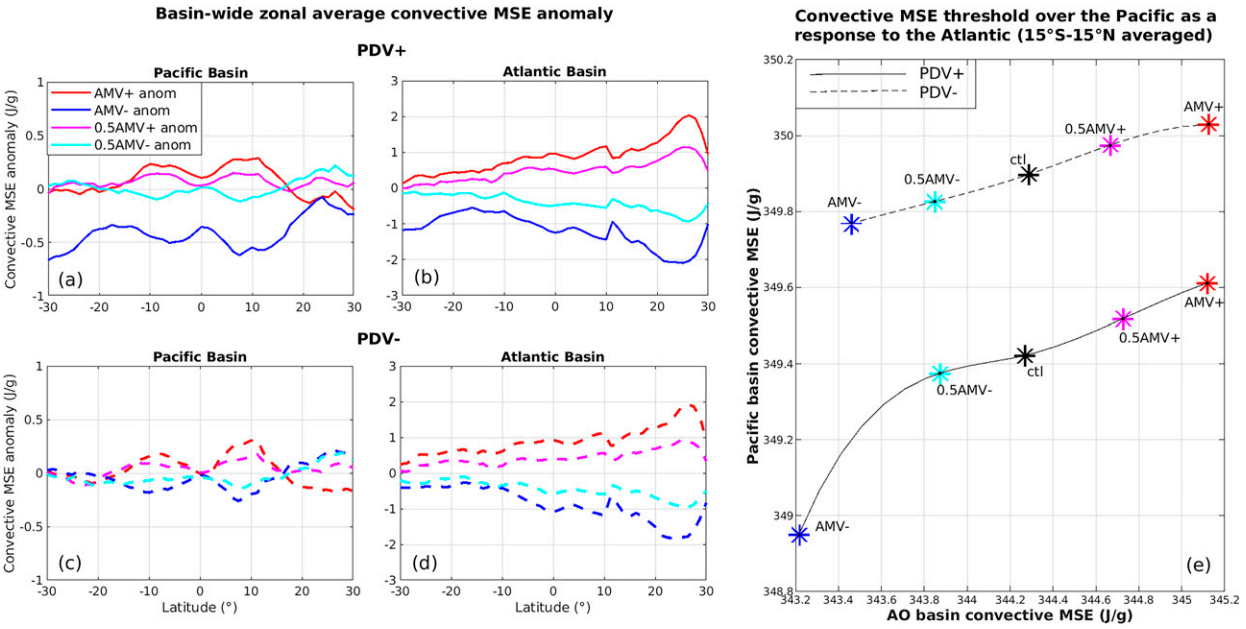


FIG. 4. Convective MSE (J $g^{-1}$) anomalies (AMV experiments minus control) in different ocean basins for all experiments as a function of latitude (30°S–30°N): Mean convective MSE anomalies of the experiments over the (left) Pacific and (center) Atlantic basins in (a),(b) PDV+ and (c),(d) PDV− phases. (e) Symbols give the basinwide convective MSE change for each experiment in the two PDV phases. In (e), the convective MSE (J $g^{-1}$) is averaged between 15°S and 15°N in each of the AMV experiments over the Pacific basin, and the TPO perturbations ($y$ axis) are presented as a function of TAO perturbation ($x$ axis). Fitted line between experiment data points (symbols) is estimated using a cubic spline.

### c. *Relationship to MSE changes*

To further quantify the remote influence of AMV on TPO precipitation, we consider the relationship between precipitation and the subcloud moist static energy (MSE). The recent study of Zhang and Fueglistaler (2020) identified subcloud MSE as a key thermodynamic indicator of the likelihood of precipitation, with precipitation increasing rapidly above a threshold MSE. In this perspective, the increased stability induced by AMV affects precipitation by increasing this MSE threshold for convection by essentially making it harder to rain. Further to this, we will also show below that the relevant MSE threshold is different in different basins, and the relative magnitude of changes in the MSE threshold for convection in the TAO and TPO provides a quantification of the influence of AMV on the Pacific.

The subcloud MSE $h$ is given by

$$h = c_p T + gz + Lq, \tag{1}$$

where $c_p$ is the specific heat capacity of air at constant pressure, $T$ is the surface air temperature, $g$ is the acceleration due to gravity, $L$ is the latent heat of vaporization of water, $q$ is the surface air–specific humidity, and $z$ is height, which we set to zero at the ocean surface. The subcloud layer is considered to be the portion of the boundary layer extending from the surface to the average height of the base of clouds (Zhang and Fueglistaler 2020; Blunden and Arndt 2012). Here, for simplicity, we take the MSE of near-surface air as representative of the subcloud MSE. This approximation has been used by a number of previous studies relating low-level MSE to precipitation (Barnes and Garstang 1982; Betts 1976; Privé and Plumb 2007).

Following Zhang and Fueglistaler (2020), we define, for a given region, the convective MSE $h_c$ as a measure of the MSE above which strong precipitation occurs. Specifically, $h_c$ is given by

$$h_c = \frac{\sum_i P_i h_i}{\sum_i P_i}, \tag{2}$$

where $P$ is the daily precipitation, and the sum is over all grid points $i$ over the region for each day in the period 1978–2001.

As expected from the SST forcing, $h_c$ increases over the TAO for AMV+ and decreases for AMV− regardless of the phase of PDV (Figs. 4b,d). This is due partly to changes in surface air temperature but mostly to changes in humidity in response to a warmer or cooler sea surface. Over the TAO, these changes are relatively linear in the magnitude of the imposed TAO anomalies, although the convective MSE response in the AMV− experiment appears to have a slightly larger magnitude than that of the AMV+ experiment.

Over the TPO, $h_c$ is also increased for AMV+ and decreased for AMV−, but the magnitude of the changes is smaller than that in the TAO (Figs. 4a,c). Since the SST in the TPO remains the same between AMV+ and AMV−, changes

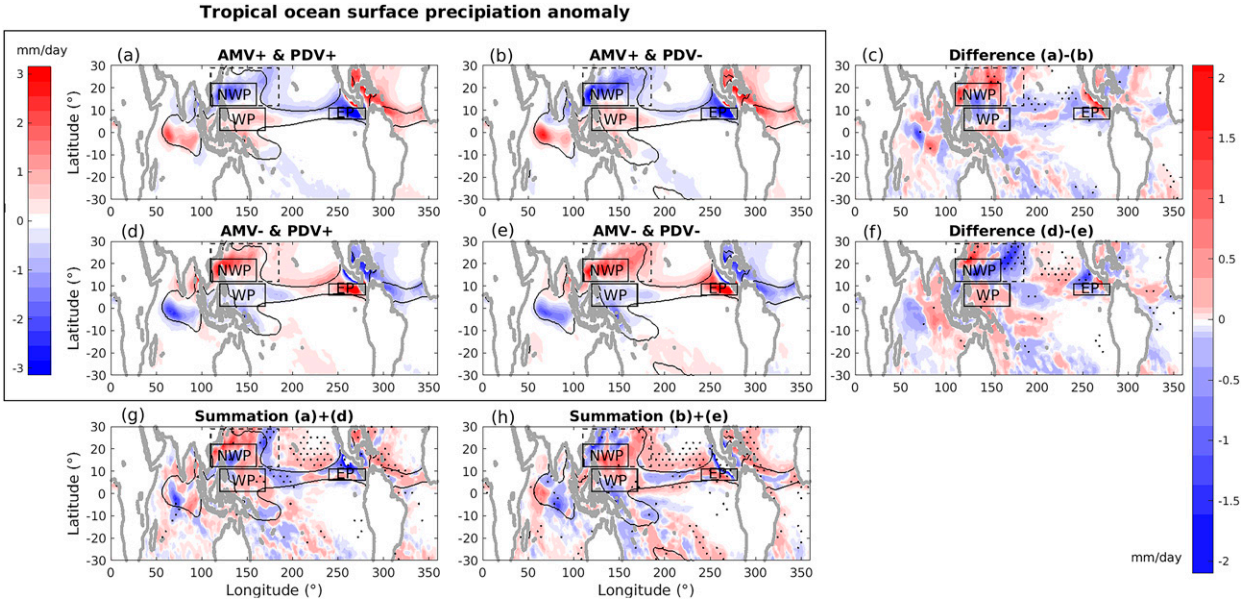


FIG. 5. JJA season mean precipitation anomaly (mm day$^{-1}$) for (a),(b) AMV+ anomaly and (d),(e) AMV− anomaly in (left) PDV+ and (center) PDV− phases. Also shown are AMV phase asymmetries for the (g) PDV+ phase and (h) PDV− phase. (right) PDV phase differences are shown for the (c) AMV+ and (f) AMV− experiments. The regions that display statistically significant rainfall differences at 95% confidence level in the asymmetry maps [i.e., (c), (f), (g) and (h)] are marked with dark gray stippling. Black-outlined regions represent the different Pacific basin regions, namely, the North-western Pacific (NWP), the Eastern Pacific (EP) and the Western Pacific (WP) regions, indicating our defined regions. Dash-outlined box corresponds to the extended NWP boxed region.

in the MSE distribution in the TPO are likely to be weak. Instead, the changes in $h_c$ are a result of changes in the distribution of precipitation, shifting toward regions with higher subcloud MSE. In other words, it could be expected that larger MSE is required to cause precipitation in the presence of a more stable atmosphere, and thus, $h_c$ is expected to increase simultaneously.

Figure 4e quantifies the relationship between $h_c$ in different ocean basins. For most experiments, an increase in the convective MSE in the Atlantic by 1 J g$^{-1}$ results in an increase in the convective MSE in the Pacific by roughly 0.2 J g$^{-1}$. The exception to this is the AMV− experiment in the PDV+ phase, in which the convective MSE in the TPO is more sensitive to decreases in TAO SSTs. This suggests a potential nonlinearity in which the ability of convection in the TAO to affect precipitation over the Pacific depends on the mean state of both the Atlantic and Pacific basins. However, it is worth noting that there does not appear to be much nonlinearity in the basinwide precipitation response seen in Fig. 2, and this is the first analysis that seems to identify nonlinearity with convective MSE where we focus on only the wet locations.

We note that the convective MSE in the TPO differs substantially between the PDV phases, but this does not lead to a substantial change in the convective MSE over the TAO. This result points to interesting differences between pantropical influences from and to the Pacific that we hope to explore in future work.

## 4. The regional rainfall response

We now endeavor to understand the spatial characteristics of the Pacific Ocean precipitation response to the AMV perturbations to check for uniformity and asymmetries. For this, we analyze spatial patterns of the AMV-induced mean precipitation anomalies in both the PDV phases in Figs. 5a,b,d,e. Consistent with the basin-averaged results presented above, TPO rainfall is generally suppressed in the AMV+ experiments and enhanced in the AMV− experiments. However, there are some regions that oppose the basinwide trends; in the west Pacific region (marked WP on Fig. 5), precipitation is enhanced in AMV+ and suppressed in AMV−. The AMV+ and AMV− experiments are largely mirror images of each other (Figs. 5g,h). However, we see a relatively small region of significant AMV phase asymmetry in the north-central/east Pacific in both Figs. 5g and 5h. Looking at the PDV phase asymmetries (Figs. 5c,f), we also see some relatively small regions of significant asymmetry in the AMV− experiment, where the regions displaying significant differences appear to have larger-magnitude anomalies in the PDV− phase, especially in the northwestern Pacific (NWP) region. Overall, these results suggest that the TPO precipitation response from the TAO appears largely insensitive to the phases of AMV and PDV.

Figure 6 displays boxplots of JJA precipitation anomalies in the different Pacific basin regions (Fig. 5), namely, the NWP (110°–160°E, 12°–22°N; Fig. 6a), NWP extended region (110°–185°E, 12°–29°N; Fig. 6b), WP (120°–170°E, 1°–11°N; Fig. 6c), and EP (80°–120°W, 6°–11°N; Fig. 6d), in the two PDV phases and in all the AMV experiments. These regions were selected because they either generally contained large precipitation anomalies or were somewhat distinct from the surrounding precipitation responses (Fig. 5). The linear

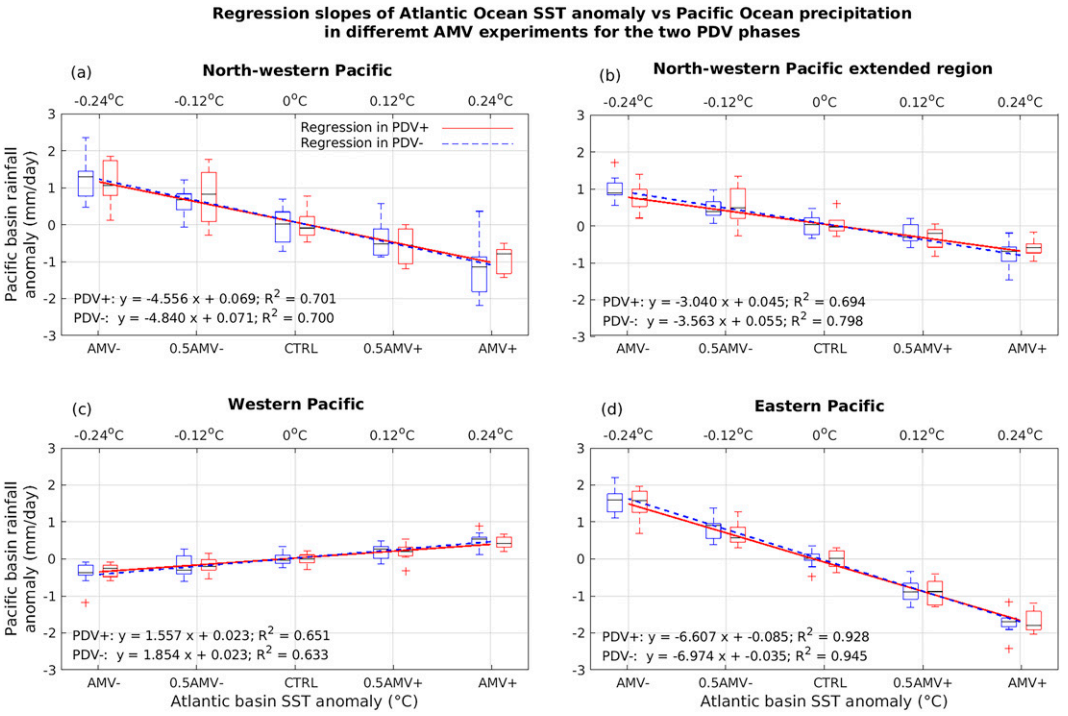


FIG. 6. Boxplots of the JJA precipitation anomalies in the different Pacific basin regions, namely, the (a) NWP (110°–160°E, 12°–22°N), (b) NWP extended region (110°–185°E, 12°–29°N), (c) WP (120°–170°E, 1°–11°N), and (d) EP (80°s–120°W, 6°–11°N), in the two PDV phases (red boxplots represent PDV+ phase in all AMV experiments, and blue boxplots represent those in PDV− phase). The median of any distribution is marked as a solid black line within the boxplots. A solid red line represents the slope of regression of Atlantic Ocean SSTAs vs the Pacific basin rainfall anomaly in all AMV experiments in PDV+ phase, and a dashed blue line represents a similar regression for the PDV− phase.

regression slopes are then calculated and plotted over the boxplots in each region. In each PDV phase, we have anomalies of five AMV experiments, each having 10 ensemble members. Thus, the total number of points with which the regression analysis is done in each PDV phase is 50. We also consider the 95% confidence level of these fitted regression lines, highlighting slope differences where the 95% confidence levels do not overlap.

We observe the smallest regression slope in the WP region and the largest regression slope in the EP region (the EP slope being almost 4 times that of the WP region), suggesting that the AMV's compensating impact on the WP rainfall is much smaller that the rainfall impacts elsewhere. Each experiment's regional median (black solid line within the boxplots) rainfall lies very close to the fitted regression lines in both the PDV phases and also displays high $R^2$ values, both of which suggest that a lot of the regional rainfall changes are explained by a linear relationship. Moreover, the similarity of the regression slopes and $R^2$ values between the different PDV phases indicates that the relationship between AMV and Pacific regional rainfall response does not differ much in the PDV phases in these different regions. Further to this, there is no statistically significant difference in the slopes of the regression lines in any of these regions between the different PDV phases (Figs. 6a–d), with the PDV− regression line slope lying between the 5th and 95th percentiles of the PDV+ slope.

## 5. The regional wind response

In this section, we seek to better understand the TPO response to AMV forcing in the context of the surface winds, since it is the surface wind and surface wind stresses that drive oceanic heat flux and circulation changes, respectively. Furthermore, much recent literature on pantropical connections has focused on the atmospheric Walker circulation surface wind response to changing TAO SSTAs (McGregor et al. 2014, 2018; Ruprich-Robert et al. 2017; Meehl et al. 2021; Chikamoto et al. 2020). It has been reported that during an Atlantic warming scenario, the Indo–western equatorial Pacific experiences anomalous easterlies driven by atmospheric Kelvin waves, whereas the eastern equatorial Pacific is impacted by westerly wind events driven by off-equatorial Rossby waves. These changes are consistent with a typical Gill-type response to Atlantic atmospheric heating perturbation (McGregor et al. 2014; Li et al. 2016). The wind–evaporation–SST feedback further intensifies the WP warming and EP cooling contributing to La Niña–like conditions over the Pacific (McGregor et al. 2014; Levine et al. 2017; Choi et al. 2019; Geng et al. 2020). The opposite TPO responses might be expected for a cool TAO (Ruprich-Robert et al. 2017).

In Fig. 7, which displays the AMV-induced wind (vectors) and wind speed (shading) anomalies in both PDV phases (Figs. 7a,b,d,e), we observe that the Southern Hemisphere

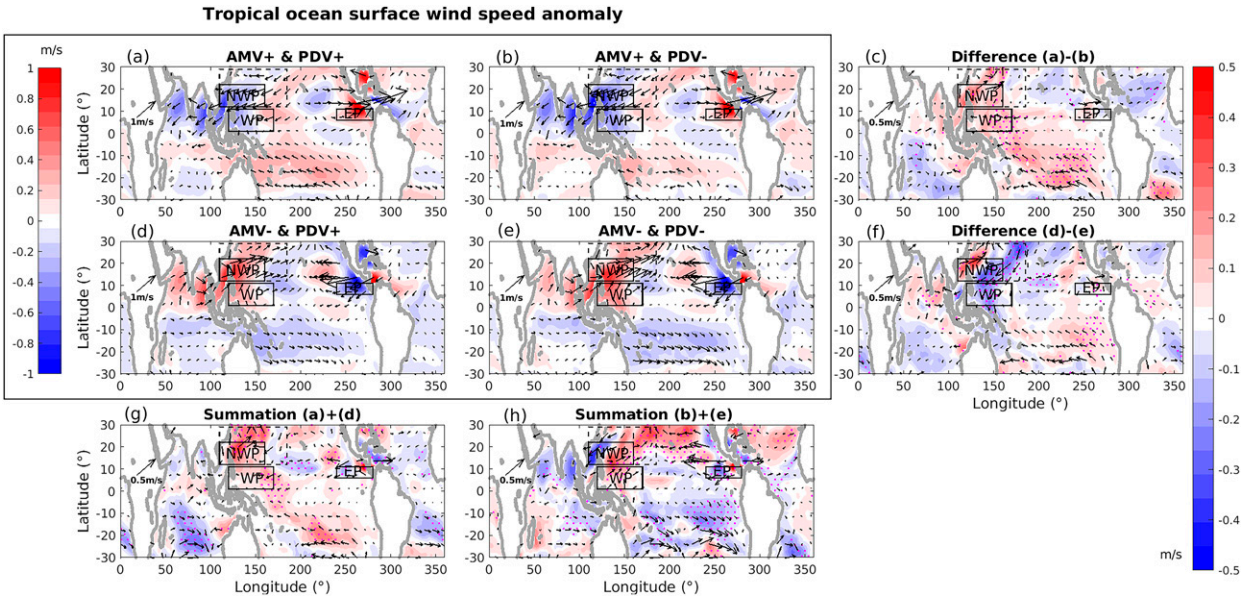


FIG. 7. As in Fig. 5, but for mean wind speed (m $s^{-1}$), and with magenta stippling.

(SH) largely displays what can be described as an intensification or damping of the trade winds, which blow from the southeast toward the northwest. This is clearly seen by the wind speed acceleration/intensification during AMV+ and deceleration/weakening during AMV−. However, the Northern Hemisphere (NH) is a little more complicated. Here, an AMV+ induces a zonal wind response composed of east-northeasterly anomalies in the west and west-northwesterly anomalies in the east. The NH wind speed response, which is more complicated than the zonal wind response because its changes are presented in relation to the climatology, reveals a quadpole structure spanning the Pacific. This AMV+ surface zonal wind and wind speed response is largely mirrored in the AMV− experiment. We also note that there is an opposite-sign zonal wind and wind speed response in the eastern and western equatorial Pacific (Figs. 7a,b,d,e), which is consistent with results reported in earlier studies on ENSO wind response (Harrison and Vecchi 1997; Harrison and Larkin 1998; Li et al. 2023).

The AMV phase asymmetry plot of the PDV+ phase (Fig. 7g) reveals that the most prominent significant differences are located in the western equatorial Pacific (particularly in the western half of the Niño-4 region), as the AMV+ wind speed modulation in this region is larger than that of AMV−. The PDV− phase–AMV phase asymmetry plot (Fig. 7h) does not reveal a similar western equatorial Pacific wind speed asymmetry (as in Fig. 7g). Here, however, the regions displaying significant AMV phase asymmetries are all off the equator. In these regions, the AMV− response has a stronger off-equatorial wind speed response larger than that of AMV+.

Focusing now on PDV phase differences in the AMV+ experiment, Fig. 7c reveals significant asymmetries largely on the equator in the western equatorial Pacific and also off the equator in the SH. The wind speed asymmetries in the western equatorial Pacific and South Pacific region both appear because the PDV+ experiment displays stronger surface wind speed changes than the PDV− experiment. Thus, PDV+ has a larger response than PDV− (enhancing the positive effect). The PDV phase asymmetry in the AMV− experiment (Fig. 7f) indicates that the significant differences are mostly off the equator. Looking at the −wind speed magnitudes induced by AMV−, PDV− appears to have a larger off-equatorial wind speed response than PDV+ in this region (enhancing the negative effect). Also, there are less significant areas here than in Fig. 7c, suggesting that the −changes induced by AMV− in the PDV− phase are less important than the changes induced by AMV+ in the PDV+ phase.

We now shift to analyze distributions of regional average zonal winds, since the zonal wind and its associated curl in the off-equatorial regions are considered to be important for driving ocean circulation changes, while higher-frequency zonal wind events in the equatorial Pacific play a role in the onset and maintenance of ENSO events (Harrison and Vecchi 1997; McGregor et al. 2016). We selected certain regions over the Pacific basin that displayed very prominent wind differences, as seen in the boxed regions in Fig. 7. Looking at the regional average distributions of daily zonal winds in JJA (Fig. 8), it is clear that the EP region shows the largest changes in the zonal wind response to AMV forcing (along with the largest differences in the peaks of the distributions). To quantify the distribution changes in each of these regions, we define the fraction of area below or above the corresponding control median zonal wind as anomalous easterly or westerly wind days, respectively. The percentage shift in the wind distributions is between 5% and 38% in the anomalous easterly or westerly wind days between the AMV experiments in these regions. In the AMV+ experiment, the NWP, NWP extended, and WP regions tend to have much more frequent easterly wind days

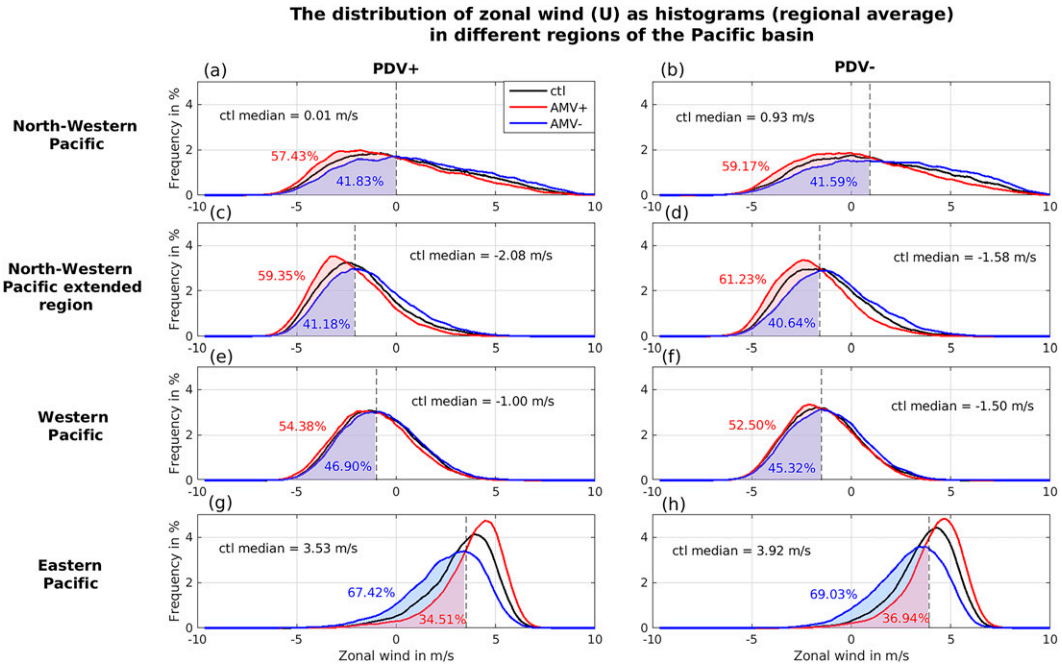


FIG. 8. Distribution of zonal wind as histograms of daily regional averages in the four different Pacific basin regions (see *y*-axis labels) for (a),(c),(e),(g) PDV+ phase and (b),(d),(f),(h) PDV− phase. Shaded regions and the associated numbers represent the percentage shift in anomalous easterly wind days between the AMV experiments.

(conversely, they are less likely to have westerly wind events) than in the AMV− experiment. For the EP region, on the other hand, the AMV+ experiment leads to a roughly 30% decrease in easterly wind days, while the AMV− experiment produces wind changes that roughly mirror these. These reported regional zonal wind changes are quite consistent in both PDV phases, suggesting little difference in the AMV response between different PDV phases.

The changes in mean wind (Fig. 7) and wind variability (Fig. 8) in our fixed-SST experiments described above would be expected to strongly affect the ocean state and its variability in a coupled system. For example, it is known that a higher incidence of westerly wind events characterizes the eastern equatorial Pacific during the peak of El-Niño (Harrison and Larkin 1998), while a band of moderate easterly anomalies stretches from the Central American coast to the ITCZ region at the same time (Harrison and Larkin 1998; Larkin and Harrison 2002). Both of these changes appear consistent with the zonal wind changes seen during our AMV−, which include anomalous easterly wind events in the EP region (Figs. 8g,h) similar to those of an El Niño–like response. Conversely, AMV+ generates anomalous westerly wind events in the EP region, which is analogous to a La Niña–like response (Figs. 8g,h). Thus, this implies that the Pacific Ocean wind changes associated with the different AMV experiments are able to provide conditions favorable for the initiation and maintenance of El Niño and/or La Niña events (Wang and Fiedler 2006; Peng et al. 2020).

As discussed above, the −surface winds induced by AMV− are broadly consistent with those that occur during a La Niña event; however, we note that the WP region previously defined is not one that is typically utilized for ENSO analyses. Previously, we observed that there are significant AMV phase asymmetries in the PDV+ phase, identified in the western half of the Niño-4 region, with AMV+ capable of imposing a stronger wind speed modulation than AMV− (Fig. 7g). Hence, now we focus on a more relevant region for ENSO, which is the western equatorial Pacific or Niño-4 region (160°E–150°W, 8°S–8°N; Fig. 9). In this region, the AMV− experiments produce positive zonal winds (westerlies) in the western equatorial Pacific (Fig. 9a), which results in weaker wind speeds because the climatological zonal winds in this region are negative (easterlies; Fig. 9b). We expect this to create El Niño–like (warming in this region) background conditions (weaker winds ≥ less latent heat loss + east Pacific thermocline deepening ≥ warming) and to weaken the Walker circulation. For AMV+, we can expect more easterlies (Fig. 9a) or stronger trade winds, thereby favoring a La Niña–like response in the Pacific by strengthening the Walker circulation (stronger winds ≥ more latent heat loss + east Pacific thermocline shoaling ≥ cooling).

Turning to the response of the Niño-4 region zonal winds to AMV in different PDV phases since this region displays very prominent wind differences (as seen in Fig. 7), we see that the regression slopes of both PDV phases (Figs. 9a,b) display significant differences, indicating that the Niño-4 region zonal wind response to AMV forcing differs substantially depending on PDV phase. For instance, variations of Niño-4 region zonal wind or wind speed anomalies with AMV phase are stronger during the PDV+ phase (i.e., a larger regression

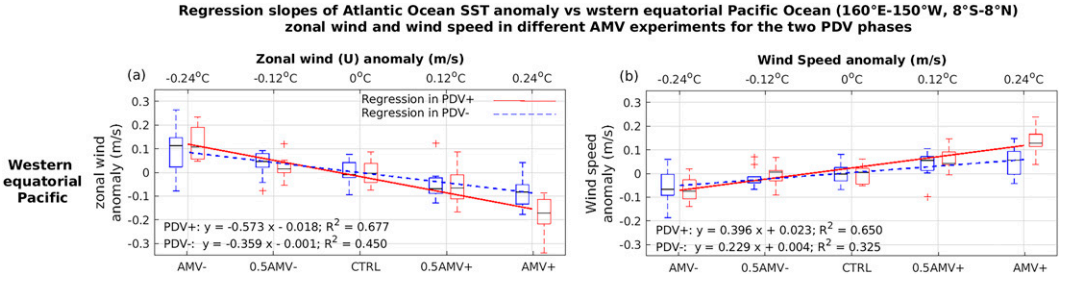


FIG. 9. Boxplots of the JJA (a) zonal wind and (b) wind speed anomalies in the western equatorial Pacific region in the two PDV phases (red boxplots represent PDV+ phase in all AMV experiments, and blue boxplots represent those in PDV− phase). The median of any distribution is marked as a solid black line within the boxplots. The solid red line across the boxplots represents the slope of regression of Atlantic Ocean SSTAs vs the Pacific basin zonal wind (or wind speed) anomaly in all AMV experiments in PDV+ phase, and the dashed blue line represents the ones in PDV− phase.

slope and $R^2$ value) than they are in the PDV− phase. In fact, the wind responses induced by AMV+ in the PDV+ phase is roughly 40% larger than that found in the PDV− phase. Also, we note that the largest PDV phase differences occur in the AMV+ phase, where the PDV+ phase median is well outside of the PDV− phase interquartile range in both the zonal winds as well as the wind speed anomalies over the western equatorial Pacific region (Fig. 9). It is this region that displays significant AMV phase asymmetries in Figs. 7c and 7g; that is, the AMV+ creates a larger Niño-4 region wind response than AMV−, while PDV+ creates a larger response than PDV−. This suggests that the phases of PDV and AMV are important for the Niño-4 region wind response.

We hypothesize that this PDV phase asymmetric surface wind response, which occurs despite minimal precipitation asymmetries, results from differences in the atmospheric boundary layer stability. It is typically thought that the troposphere is the source of momentum, while the surface is typically a momentum sink; thus, changes in this connectivity may be able to explain the PDV phase surface wind asymmetries seen in our experiments. To examine this, we follow the work of van Rensch et al. (2022) and calculate the correlation/regression between the control simulation monthly zonal winds at the 850-hPa level and those at the surface for the western Pacific region in the two PDV phases separately (figure not shown). Results from this analysis reveal that the regression relationship between the 850-hPa zonal wind versus surface zonal wind response is quite distinct in the two PDV phases [when considering the 95% confidence level of these fitted regression lines, the slopes do not overlap, indicating a statistically significant difference (not shown)]. That is, the PDV+ phase displays a steeper/stronger slope than that of PDV−, suggesting that a given change in 850-hPa zonal wind will drive a stronger surface wind response in the PDV+ phase than the same change in 850-hPa wind would during the PDV− phase.

It is interesting that this is the way the climate system transitioned from the 1990s into the 2000 period; that is, in the 1990s, AMV was warming while PDV was in a positive phase. This could provide a hypothesis for the changing influence of the different ocean basins in the recent period after 1990, where it is seen that the TAO influence on the TPO is much more pronounced than that of the TIO on the TPO (Cai et al. 2019).

Literature suggests that ENSO is sensitive to the background-state thermocline depth, with its zonal mean (McPhaden et al. 2006; Neelin et al. 1998; Fedorov and Philander 2000; Zhang et al. 1997) and tilt potentially playing a modulating role (Yeh et al. 2009; Capotondi and Sardeshmukh 2015). As such, the TPO response to AMV is further investigated with a linear ocean "shallow water" model (SWM; McGregor et al. 2007; Neske and McGregor 2018) forced with a repeating anomalous annual cycle of wind stresses from the four AMV experiments ($\alpha = -1, -0.5, 0.5$, and 1) for each PDV phase for 20 yr. The SWM is a linear (two dimensional) first baroclinic-mode (shallow water) ocean model in which the wind stress–driven active upper layer is separated from the infinitely deep motionless lower layer by a sharp tropical pycnocline, which is taken to approximate the tropical Pacific thermocline. As such, the modeled changes in the zonal average equatorial thermocline could underpin changes in ENSO (Fedorov and Philander 2000), and the central Pacific thermocline depth changes could influence the ENSO event flavor (Capotondi and Sardeshmukh 2015), while the eastern Pacific thermocline depth changes may be directly related to changes in the overlying SSTs, as there is a clear direct connection with the SSTs overlying the region (Zelle et al. 2004).

In our experiments, we see that the added AMV forcing modulates the zonal mean thermocline depth. For instance, in response to the AMV+ forcing, the SWM thermocline depth is largely shallowed throughout the equatorial Pacific, with maximum shallowness in the central Pacific region (Figs. 10a,b). As such, the zonal mean changes may lead to changes in the characteristics of ENSO, while the central Pacific maximum may influence the flavor of ENSO. However, since we also have reduced thermocline depths in the eastern Pacific, we would expect to see a direct overlying SST cooling that would combine with the wind speed–driven SST changes to initiate a Bjerknes-type atmospheric feedback that amplifies the original cooling signal. On the contrary, in AMV−, the zonal mean thermocline is deeper, where the largest deviations are again seen in the central Pacific (Figs. 10c,d), again suggesting that we may see changes in ENSO properties and flavors in response to this

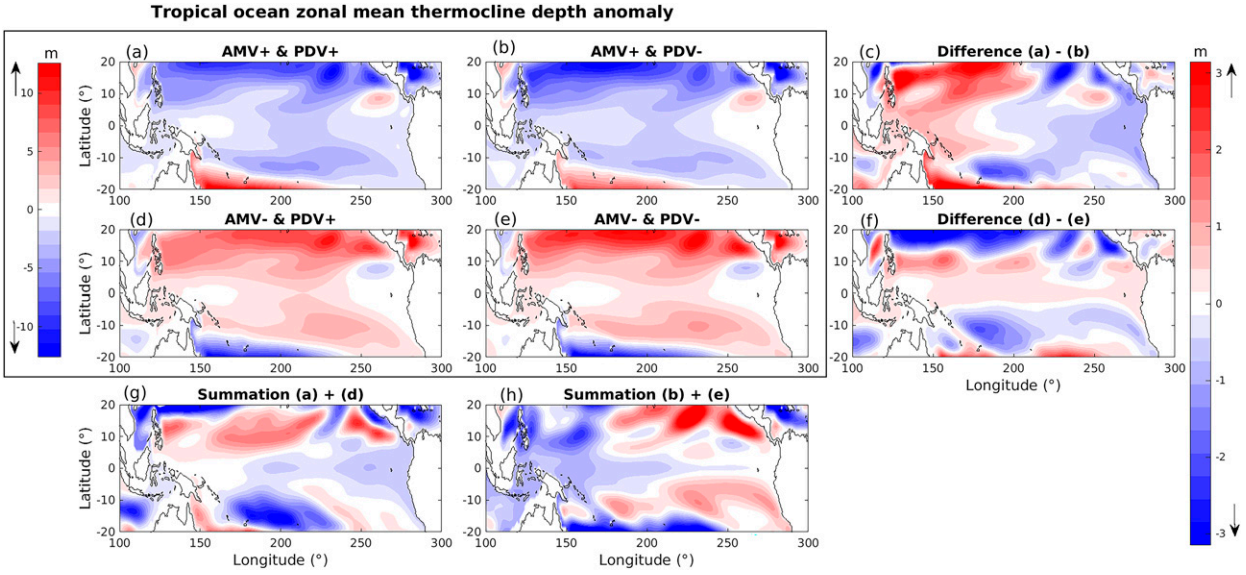


FIG. 10. SWM JJA season mean thermocline depth in (a),(b) AMV+ anomaly and (d),(e) AMV− anomaly in (left) PDV+ and (center) PDV− phases. Also shown are AMV phase asymmetries in the (g) PDV+ phase and (h) PDV− phase and PDV phase differences in the (c) AMV+ experiments and (f) AMV− experiments.

forcing. Furthermore, we would expect the thermocline depth changes in the east along with the overlying wind speed weakening to combine, leading to a warming that would again be amplified by an atmospheric Bjerknes-type response.

In both Figs. 10g and 10h, which show the AMV phase asymmetries, we see that AMV+ impacts are more pronounced on the equator than those of AMV−. However, there are differences in the longitudinal regions influenced. For instance, the PDV+ phase shows the largest asymmetries in the central/eastern Pacific, consistent with the western equatorial region zonal wind asymmetries identified (Fig. 7), while the PDV− phase displays the largest asymmetries in the western/central Pacific, which appears to be related to off-equatorial zonal wind asymmetries altering the wind stress curl. Both AMV phases also display some PDV phase thermocline depth asymmetries (Figs. 10c,f), but the most prominent is the pronounced zonal thermocline depth tilt seen in the AMV+ phase (Fig. 10c). Here, PDV+ displays the largest thermocline depth shallowing in the east, consistent with the enhanced western equatorial Pacific zonal wind strengthening (Fig. 7), while PDV− displays a larger deepening thermocline in the west, which is consistent with the stronger off-equatorial wind response altering the wind stress curl.

## 6. Conclusions

Motivated by observed decadal variations in interbasin interactions affecting the Pacific, this study used AMIP-style simulations to probe the response of the Pacific to different phases and magnitudes of AMV. Specifically, we investigated the extent to which the atmospheric response was asymmetric with respect to the sign of AMV. We further investigated if these responses were affected by the phase of PDV.

Our analysis focuses on the Pacific precipitation and surface wind response. The focus on the former is mainly because the nonlinearities in precipitation formation make it a likely candidate to display AMV and PDV phase asymmetries. The focus on the latter is because surface winds, both speed and direction, play a fundamental role in ocean dynamics, SST changes, and ocean–atmosphere coupling. As such, in the fully coupled system, changes in wind speed, for instance, lead to changes in the surface latent and sensible heat fluxes, while changes in wind direction and structure can drive dynamical oceanic responses that can be important for setting the background state of ENSO.

Our results reveal that in both PDV phases, the AMV+ experiments suppress TPO precipitation, while the AMV− experiments enhance TPO precipitation, although there is a substantial spatial structure to these changes, with rainfall in the WP opposing the basinwide response. Despite the complexity of the rainfall response, the different phases of AMV produce rainfall patterns that largely mirror each other, and there is little phase asymmetry in the AMV response. Similarly, the TPO rainfall response to AMV is largely independent of PDV phase.

The basinwide response of the TPO to AMV is related to changes in stability in the TPO induced by surface and atmospheric warming/cooling over the TAO. Specifically, for AMV+, warming in the TAO is communicated to the TPO by atmospheric waves. Since the SST in the TPO remains unchanged, this results in a stabilization of the troposphere, which tends to suppress precipitation. An analogous chain may be constructed for the AMV− case. These results are consistent with simple models of the wave response of the atmosphere to diabatic heating anomalies (e.g., Gill 1980; Sobel et al. 2001).

The changes in Pacific rainfall may alternatively be interpreted as being a response to an increased threshold for

convection, quantified here by the "convective MSE," defined as the precipitation-weighted MSE averaged over the basin. Increasing the TAO temperature (AMV+) leads to an increase in the convective MSE required for rainfall over the TPO, essentially making it more difficult to rain. The opposite is largely seen with decreasing TAO SSTs (AMV−). This analysis gave us our first glimpse at nonuniform changes between the AMV experiments in the two PDV phases. That is, we saw much larger TPO MSE changes for the AMV− experiment in the PDV+ phase than we did in any of the other experiment configurations. In fact, outside of this, the TPO MSE changes appeared to scale almost linearly with AMV forcing (Fig. 4e). Understanding this apparent nonlinearity and the MSE relationship to actual average TPO precipitation changes, which appear to scale linearly with AMV forcing, is a topic that requires further exploration in a future study. It was also interesting to note that the MSE threshold for the TPO and TAO appears to be different, suggesting that simply identifying a tropical convective MSE, as has been done in recent studies (Zhang and Fueglistaler 2020), may miss important pantropical differences.

In contrast to the rainfall changes, important phase asymmetries are found for the wind response to AMV. First, however, we see that the anomalous winds induced with AMV+ forcing are smaller but consistent in sign with those of a La Niña event (Figs. 7d,e), while those induced with AMV− forcing are consistent with those of an El Niño event (Figs. 7a,b). These wind changes are largely consistent with those reported in earlier studies on ENSO wind response (Harrison and Vecchi 1997; Harrison and Larkin 1998; Zhao and Fedorov 2020; Neske et al. 2021). However, looking at the asymmetric response with respect to different AMV scenarios has not been explored in previous studies. For instance, we have seen that in the PDV+ phase, significant AMV phase asymmetries are located in the western half of the Niño-4 region, with the AMV+ wind speed modulation in this region being larger than that of AMV− (Fig. 7g). Moreover, we have found that the western equatorial Pacific (or Niño-4 region) trade wind intensification induced by AMV+ in the PDV+ phase is significantly larger than the western equatorial Pacific trade wind response induced by AMV+ found during the PDV− phase (Fig. 9a). In fact, the zonal wind and wind speed responses induced by AMV+ in PDV+ are roughly 40% larger than those in the PDV− phase. Combined, these suggest that the western equatorial Pacific wind response to AMV+ forcing in the PDV+ phase has a larger magnitude than the wind changes found in any other combination of AMV and PDV phases. Moreover, the regression relationship between the 850-hPa zonal wind versus surface zonal wind response in the western equatorial Pacific suggests that a given change in 850-hPa zonal wind will drive a stronger surface wind response in the PDV+ phase than that during the PDV− phase.

We also analyzed the daily regional mean zonal wind distributions, since zonal wind variability is considered to be important for the initiation, maintenance, and termination of ENSO (Bjerknes 1969; Philander 1983; Trenberth and Hoar 1997; Fedorov and Philander 2000; McPhaden et al. 2006; Timmermann et al. 2018). Our experiments suggest that in both the PDV phases, an AMV+ scenario leads to a substantial increase in westerly wind events in the EP (Figs. 8g,h) and a substantial increase in easterly wind events in the WP (Figs. 8e,f). During an AMV− phase, the wind response in both regions is almost mirrored (Figs. 8e–h). Furthermore, in an AMV+ anomaly, the strong trade winds in the Niño-4 region (Fig. 9a) and enhanced wind speeds (Fig. 9b) will contribute to more latent heat loss and hence more warming. Thus, we can expect strengthening of the Walker circulation that can further create background conditions favorable for La Niña events to occur. Conversely, for AMV− experiments, anomalous westerlies are seen in the western equatorial Pacific (Fig. 9a), along with weaker wind speeds (Fig. 9b), favoring an El Niño–like response in the Pacific by weakening the Walker circulation (i.e., weaker winds would result in less latent heat loss and hence more warming).

While our GCM experiments use fixed SSTs and therefore do not simulate oceanic dynamics, the simulated wind stress anomalies imply background-state changes in the ocean state that may have implications for ENSO behavior under different phases of decadal variability. Initial investigations with a linear oceanic shallow water model forced by the AGCM-simulated wind stress patterns show that the AMV-induced changes modulate the zonal mean thermocline depth, where zonal mean thermocline depth is shallower in the AMV+ phase and deeper in the AMV− phase, and that the changes are most prominent in the central Pacific (Figs. 10a,b,d,e). The central and eastern Pacific changes would be expected to directly relate to anomalous SSTs due to the tight connection between these two variables (Zelle et al. 2004), with the shallower thermocline depths during AMV+ phases also leading to reduced SSTAs. On the other hand, lower-complexity models of ENSO suggest that changes in the zonal mean thermocline depth are related to the ENSO period, where a shallower thermocline depth would be generally expected to lead to a higher frequency of ENSO occurrence (Fedorov and Philander 2000). The prominent surface wind asymmetries reported above also appear to drive prominent asymmetries in the oceanic thermocline response (Figs. 10c,f,g,h), which may also lead to asymmetries in any induced ENSO behavior changes.

Thus, by thoroughly exploring asymmetries in the precipitation and surface wind responses to AMV forcing, we have identified several factors that could help to explain the increasing prominence of the TAO–TPO pantropical connection. First, our results show that the pantropical Atlantic–Pacific connection is stronger for the AMV+ and PDV+ phases, which are the warming phases consistent with those observed around the year 2000, as suggested by the zonal wind and wind speed responses in the western Pacific (Figs. 7g,h and 9a,b). Although it is unclear precisely how much impact these apparent asymmetries would have on the TPO, the asymmetries identified here may be able to explain at least some portion of the recent observed increase in TAO prominence. This is a single-model study and may need confirmation with other models. Also, as these experiments are performed with respect to a fixed SST, any coupled response is hypothetical for now. We also note that to fully answer this question, we

need to also understand how the TIO influences the TPO. However, this question is beyond the scope of the current paper and is the focus of separate additional work that will be covered in a future article.

*Acknowledgments.* All authors acknowledge the ARC Centre of Excellence for Climate Extremes (Grant CE170100023) for supporting this research. Shayne McGregor acknowledges support from the ARC through Grants FT160100162 and DP200102329. Martin Singh acknowledges support from the ARC through Grants DE190100866 and DP200102954. This research was undertaken with the assistance of resources and services from the NCI, which is supported by the Australian government. We thank all three reviewers and the editor for their very thoughtful and constructive feedback on this paper. The authors have no conflicts to disclose.

*Data availability statement.* The data and scripts used in this work are available from the corresponding author upon reasonable request.

## REFERENCES

Barnes, G. M., and M. Garstang, 1982: Subcloud layer energetics of precipitating convection. *Mon. Wea. Rev.*, **110**, 102–117, https://doi.org/10.1175/1520-0493(1982)110<0102:SLEOPC>2.0.CO;2.

Betts, A. K., 1976: The thermodynamic transformation of the tropical subcloud layer by precipitation and downdrafts. *J. Atmos. Sci.*, **33**, 1008–1020, https://doi.org/10.1175/1520-0469(1976)033<1008:TTTOTT>2.0.CO;2.

Bi, D., and Coauthors, 2013: The access coupled model: Description, control climate and evaluation. *Aust. Meteor. Oceanogr. J.*, **63**, 41–64, https://doi.org/10.22499/2.6301.004.

Bjerknes, J., 1969: Atmospheric teleconnections from the equatorial Pacific. *Mon. Wea. Rev.*, **97**, 163–172, https://doi.org/10.1175/1520-0493(1969)097<0163:ATFTEP>2.3.CO;2.

Blunden, J., and D. S. Arndt, 2012: State of the Climate in 2011. *Bull. Amer. Meteor. Soc.*, **93** (7), S1–S282, https://doi.org/10.1175/2012BAMSStateoftheClimate.1.

Bretherton, C. S., and A. H. Sobel, 2003: The Gill model and the weak temperature gradient approximation. *J. Atmos. Sci.*, **60**, 451–460, https://doi.org/10.1175/1520-0469(2003)060<0451:TGMATW>2.0.CO;2.

Cai, W., P. Whetton, and A. Pittock, 2001: Fluctuations of the relationship between ENSO and northeast Australian rainfall. *Climate Dyn.*, **17**, 421–432, https://doi.org/10.1007/PL00013738.

——, and Coauthors, 2019: Pantropical climate interactions. *Science*, **363**, eaav4236, https://doi.org/10.1126/science.aav4236.

Capotondi, A., and P. D. Sardeshmukh, 2015: Optimal precursors of different types of ENSO events. *Geophys. Res. Lett.*, **42**, 9952–9960, https://doi.org/10.1002/2015GL066171.

Chikamoto, Y., T. Mochizuki, A. Timmermann, M. Kimoto, and M. Watanabe, 2016: Potential tropical Atlantic impacts on Pacific decadal climate trends. *Geophys. Res. Lett.*, **43**, 7143–7151, https://doi.org/10.1002/2016GL069544.

——, Z. Johnson, S.-Y. S. Wang, M. McPhaden, and T. Mochizuki, 2020: El Niño–Southern Oscillation evolution modulated by Atlantic forcing. *J. Geophys. Res. Oceans*, **125**, e2020JC016318, https://doi.org/10.1029/2020JC016318.

Choi, J.-Y., Y.-G. Ham, and S. McGregor, 2019: Atlantic–Pacific SST gradient change responsible for the weakening of north tropical Atlantic–ENSO relationship due to global warming. *Geophys. Res. Lett.*, **46**, 7574–7582, https://doi.org/10.1029/2019GL082804.

Ding, R., and Coauthors, 2023: North Atlantic Oscillation controls multidecadal changes in the north tropical Atlantic–Pacific connection. *Nat. Commun.*, **14**, 862, https://doi.org/10.1038/s41467-023-36564-3.

Dommenget, D., and Y. Yu, 2017: The effects of remote SST forcings on ENSO dynamics, variability and diversity. *Climate Dyn.*, **49**, 2605–2624, https://doi.org/10.1007/s00382-016-3472-1.

England, M. H., and Coauthors, 2014: Recent intensification of wind-driven circulation in the Pacific and the ongoing warming hiatus. *Nat. Climate Change*, **4**, 222–227, https://doi.org/10.1038/nclimate2106.

Fedorov, A. V., and S. G. Philander, 2000: Is El Niño changing? *Science*, **288**, 1997–2002, https://doi.org/10.1126/science.288.5473.1997.

Geng, X., W. Zhang, F.-F. Jin, M. F. Stuecker, and A. F. Levine, 2020: Modulation of the relationship between ENSO and its combination mode by the Atlantic multidecadal oscillation. *J. Climate*, **33**, 4679–4695, https://doi.org/10.1175/JCLI-D-19-0740.1.

Gill, A. E., 1980: Some simple solutions for heat-induced tropical circulation. *Quart. J. Roy. Meteor. Soc.*, **106**, 447–462, https://doi.org/10.1002/qj.49710644905.

Ham, Y.-G., J.-S. Kug, J.-Y. Park, and F.-F. Jin, 2013: Sea surface temperature in the north tropical Atlantic as a trigger for El Niño/Southern Oscillation events. *Nat. Geosci.*, **6**, 112–116, https://doi.org/10.1038/ngeo1686.

Harrison, D., and G. A. Vecchi, 1997: Westerly wind events in the tropical Pacific, 1986–95. *J. Climate*, **10**, 3131–3156, https://doi.org/10.1175/1520-0442(1997)010<3131:WWEITT>2.0.CO;2.

——, and N. K. Larkin, 1998: El Niño–Southern Oscillation sea surface temperature and wind anomalies, 1946–1993. *Rev. Geophys.*, **36**, 353–399, https://doi.org/10.1029/98RG00715.

Karamperidou, C., and Coauthors, 2020: ENSO in a changing climate: Challenges, paleo-perspectives, and outlook. *El Niño Southern Oscillation in a Changing Climate, Geophys. Monogr.,* Vol. 253, Amer. Geophys. Union, 471–484.

Kosaka, Y., and S.-P. Xie, 2013: Recent global-warming hiatus tied to equatorial Pacific surface cooling. *Nature*, **501**, 403–407, https://doi.org/10.1038/nature12534.

Kug, J.-S., and I.-S. Kang, 2006: Interactive feedback between ENSO and the Indian Ocean. *J. Climate*, **19**, 1784–1801, https://doi.org/10.1175/JCLI3660.1.

Larkin, N. K., and D. Harrison, 2002: ENSO warm (El Niño) and cold (La Niña) event life cycles: Ocean surface anomaly patterns, their symmetries, asymmetries, and implications. *J. Climate*, **15**, 1118–1140, https://doi.org/10.1175/1520-0442(2002)015<1118:EWENOA>2.0.CO;2.

Levine, A. F., M. J. McPhaden, and D. M. Frierson, 2017: The impact of the AMO on multidecadal ENSO variability. *Geophys. Res. Lett.*, **44**, 3877–3886, https://doi.org/10.1002/2017GL072524.

Li, X., S.-P. Xie, S. T. Gille, and C. Yoo, 2016: Atlantic-induced pan-tropical climate change over the past three decades. *Nat. Climate Change*, **6**, 275–279, https://doi.org/10.1038/nclimate2840.

——, X. Wang, T. Lian, N. C. Johnson, J. Zhu, C.-H. Chang, H. Liu, and W. Wang, 2021: Local and remote SST variability contribute to the westward shift of the Pacific Walker circulation during 1979–2015. *Geosci. Lett.*, **8**, 16, https://doi.org/10.1186/s40562-021-00180-0.

Li, Y., and Coauthors, 2023: Interannual variability of regional Hadley circulation and El Niño interaction. *Geophys. Res. Lett.*, **50**, e2022GL102016, https://doi.org/10.1029/2022GL102016.

Luo, J.-J., W. Sasaki, and Y. Masumoto, 2012: Indian Ocean warming modulates Pacific climate change. *Proc. Natl. Acad. Sci. USA*, **109**, 18 701–18 706, https://doi.org/10.1073/pnas.1210239109.

Maher, N., A. S. Gupta, and M. H. England, 2014: Drivers of decadal hiatus periods in the 20th and 21st centuries. *Geophys. Res. Lett.*, **41**, 5978–5986, https://doi.org/10.1002/2014GL060527.

——, D. Matei, S. Milinski, and J. Marotzke, 2018: ENSO change in climate projections: Forced response or internal variability? *Geophys. Res. Lett.*, **45**, 11 –390–11 398, https://doi.org/10.1029/2018GL079764.

Mantua, N. J., and S. R. Hare, 2002: The Pacific decadal oscillation. *J. Oceanogr.*, **58**, 35–44, https://doi.org/10.1023/A:1015820616384.

McGregor, S., N. J. Holbrook, and S. B. Power, 2007: Interdecadal sea surface temperature variability in the equatorial Pacific Ocean. Part I: The role of off-equatorial wind stresses and oceanic Rossby waves. *J. Climate*, **20**, 2643–2658, https://doi.org/10.1175/JCLI4145.1.

——, A. Timmermann, M. F. Stuecker, M. H. England, M. Merrifield, F.-F. Jin, and Y. Chikamoto, 2014: Recent Walker circulation strengthening and Pacific cooling amplified by Atlantic warming. *Nat. Climate Change*, **4**, 888–892, https://doi.org/10.1038/nclimate2330.

——, ——, F.-F. Jin, and W. S. Kessler, 2016: Charging El Niño with off-equatorial westerly wind events. *Climate Dyn.*, **47**, 1111–1125, https://doi.org/10.1007/s00382-015-2891-8.

——, M. F. Stuecker, J. B. Kajtar, M. H. England, and M. Collins, 2018: Model tropical Atlantic biases underpin diminished Pacific decadal variability. *Nat. Climate Change*, **8**, 493–498, https://doi.org/10.1038/s41558-018-0163-4.

McPhaden, M. J., S. E. Zebiak, and M. H. Glantz, 2006: ENSO as an integrating concept in earth science. *Science*, **314**, 1740–1745, https://doi.org/10.1126/science.1132588.

——, T. Lee, S. Fournier, and M. A. Balmaseda, 2020: ENSO observations. *El Niño Southern Oscillation in a Changing Climate, Geophys. Monogr.,* Vol. 253, Amer. Geophys. Union, 39–63.

Meehl, G. A., and Coauthors, 2021: Atlantic and Pacific tropics connected by mutually interactive decadal-timescale processes. *Nat. Geosci.*, **14**, 36–42, https://doi.org/10.1038/s41561-020-00669-x.

Neelin, J. D., D. S. Battisti, A. C. Hirst, F.-F. Jin, Y. Wakata, T. Yamagata, and S. E. Zebiak, 1998: ENSO theory. *J. Geophys. Res.*, **103**, 14 261–14 290, https://doi.org/10.1029/97JC03424.

Neske, S., and S. McGregor, 2018: Understanding the warm water volume precursor of ENSO events and its interdecadal variation. *Geophys. Res. Lett.*, **45**, 1577–1585, https://doi.org/10.1002/2017GL076439.

——, ——, M. Zeller, and D. Dommenget, 2021: Wind spatial structure triggers ENSO's oceanic warm water volume changes. *J. Climate*, **34**, 1985–1999, https://doi.org/10.1175/JCLI-D-20-0040.1.

Newman, M., and Coauthors, 2016: The Pacific decadal oscillation, revisited. *J. Climate*, **29**, 4399–4427, https://doi.org/10.1175/JCLI-D-15-0508.1.

Ohba, M., and H. Ueda, 2007: An impact of SST anomalies in the Indian Ocean in acceleration of the El Niño to La Niña transition. *J. Meteor. Soc. Japan*, **85**, 335–348, https://doi.org/10.2151/jmsj.85.335.

Peng, Q., S.-P. Xie, D. Wang, Y. Kamae, H. Zhang, S. Hu, X.-T. Zheng, and W. Wang, 2020: Eastern Pacific wind effect on the evolution of El Niño: Implications for ENSO diversity. *J. Climate*, **33**, 3197–3212, https://doi.org/10.1175/JCLI-D-19-0435.1.

Philander, S. G. H., 1983: El Niño Southern Oscillation phenomena. *Nature*, **302**, 295–301, https://doi.org/10.1038/302295a0.

Power, S., and Coauthors, 2021: Decadal climate variability in the tropical Pacific: Characteristics, causes, predictability, and prospects. *Science*, **374**, eaay9165, https://doi.org/10.1126/science.aay9165.

Privé, N. C., and R. A. Plumb, 2007: Monsoon dynamics with interactive forcing. Part I: Axisymmetric studies. *J. Atmos. Sci.*, **64**, 1417–1430, https://doi.org/10.1175/JAS3916.1.

Ruprich-Robert, Y., R. Msadek, F. Castruccio, S. Yeager, T. Delworth, and G. Danabasoglu, 2017: Assessing the climate impacts of the observed Atlantic multidecadal variability using the GFDL CM2.1 and NCAR CESM1 global coupled models. *J. Climate*, **30**, 2785–2810, https://doi.org/10.1175/JCLI-D-16-0127.1.

Sobel, A. H., J. Nilsson, and L. M. Polvani, 2001: The weak temperature gradient approximation and balanced tropical moisture waves. *J. Atmos. Sci.*, **58**, 3650–3665, https://doi.org/10.1175/1520-0469(2001)058<3650:TWTGAA>2.0.CO;2.

Taylor, K. E., D. Williamson, and F. Zwiers, 2000: The sea surface temperature and sea-ice concentration boundary conditions for AMIP II simulations. PCDMI Rep. 60, 29 pp., https://pcmdi.llnl.gov/report/pdf/60.pdf?id=94.

Timmermann, A., J. Oberhuber, A. Bacher, M. Esch, M. Latif, and E. Roeckner, 1999: Increased El Niño frequency in a climate model forced by future greenhouse warming. *Nature*, **398**, 694–697, https://doi.org/10.1038/19505.

——, and Coauthors, 2018: El Niño–Southern Oscillation complexity. *Nature*, **559**, 535–545, https://doi.org/10.1038/s41586-018-0252-6.

Trenberth, K. E., and T. J. Hoar, 1997: El Niño and climate change. *Geophys. Res. Lett.*, **24**, 3057–3060, https://doi.org/10.1029/97GL03092.

van Rensch, P., S. McGregor, and D. Dommenget, 2022: Exploration of atmosphere-only model deficiencies in reproducing the 1992–2011 Pacific trade wind acceleration. *Geophys. Res. Lett.*, **49**, e2022GL099981, https://doi.org/10.1029/2022GL099981.

Wang, B., X. Luo, Y.-M. Yang, W. Sun, M. A. Cane, W. Cai, S.-W. Yeh, and J. Liu, 2019: Historical change of El Niño properties sheds light on future changes of extreme El Niño. *Proc. Natl. Acad. Sci. USA*, **116**, 22 512–22 517, https://doi.org/10.1073/pnas.1911130116.

Wang, C., and P. C. Fiedler, 2006: ENSO variability and the eastern tropical Pacific: A review. *Prog. Oceanogr.*, **69**, 239–266, https://doi.org/10.1016/j.pocean.2006.03.004.

Wang, L., J.-Y. Yu, and H. Paek, 2017: Enhanced biennial variability in the Pacific due to Atlantic capacitor effect. *Nat. Commun.*, **8**, 14887, https://doi.org/10.1038/ncomms14887.

Yeh, S.-W., J.-S. Kug, B. Dewitte, M.-H. Kwon, B. P. Kirtman, and F.-F. Jin, 2009: El Niño in a changing climate. *Nature*, **461**, 511–514, https://doi.org/10.1038/nature08316.

Yun, K.-S., and A. Timmermann, 2018: Decadal monsoon-ENSO relationships reexamined. *Geophys. Res. Lett.*, **45**, 2014–2021, https://doi.org/10.1002/2017GL076912.

Zelle, H., G. Appeldoorn, G. Burgers, and G. J. van Oldenborgh, 2004: The relationship between sea surface temperature and thermocline depth in the eastern equatorial Pacific. *J. Phys. Oceanogr.*, **34**, 643–655, https://doi.org/10.1175/2523.1.

Zhang, Y., and S. Fueglistaler, 2020: How tropical convection couples high moist static energy over land and ocean. *Geophys. Res. Lett.*, **47**, e2019GL086387, https://doi.org/10.1029/2019GL086387.

——, J. M. Wallace, and D. S. Battisti, 1997: ENSO-like interdecadal variability: 1900–93. *J. Climate*, **10**, 1004–1020, https://doi.org/10.1175/1520-0442(1997)010<1004:ELIV>2.0.CO;2.

Zhao, B., and A. Fedorov, 2020: The effects of background zonal and meridional winds on ENSO in a coupled GCM. *J. Climate*, **33**, 2075–2091, https://doi.org/10.1175/JCLI-D-18-0822.1.